# Multiple Charge Transfer States in Donor-Acceptor Heterojunctions with Large Frontier Orbital Energy Offsets

Saeed-Uz-Zaman Khan[1], Giacomo Londi[2], Xiao Liu[1], Michael A. Fusella[1], Gabriele D'Avino[3], Luca Muccioli[4,5], Alyssa N. Brigeman[6], Bjoern Niesen[7], Terry Chien-Jen Yang[7], Yoann Olivier[2], Jordan T. Dull[1], Noel C. Giebink[6], David Beljonne[2], and Barry P. Rand[1,8]

[1]Department of Electrical Engineering, Princeton University, Princeton, NJ, 08544, United States
[2]Laboratory for Chemistry of Novel Materials, University of Mons, Place du Parc 20, 7000 Mons, Belgium
[3]Institut Néel, CNRS and Grenoble Alpes University, F-38042 Grenoble, France
[4]Dipartimento di Chimica Industriale "Toso Montanari", Università di Bologna, I-40136, Bologna, Italy
[5]Institut des Sciences Moléculaires, UMR 5255, University of Bordeaux, F- 33405 Talence, France
[6]Department of Electrical Engineering, The Pennsylvania State University, University Park, Pennsylvania 16802, USA
[7]Photovoltaics and Thin-Film Electronics Laboratory, Institute of Microengineering (IMT), Ecole Polytechnique Fédérale de Lausanne (EPFL), Maladière 71, Neuchâtel 2000, Switzerland
[8]Andlinger Center for Energy and the Environment, Princeton University, Princeton, New Jersey 08544, USA

## Supplementary Information

## Device Fabrication and Characterization

**Table S1.** Molecular structures and energetics of the organic small molecule and polymer materials used in this work. All donor (D) and acceptor (A) materials have $E_g$ (HOMO-LUMO gap) > 3 eV. All the donor materials have similar ionization potential (IP), while the acceptor materials are chosen to have large electron affinity (EA), which results in very small donor HOMO-acceptor LUMO differences compared to $E_g$ of individual molecules.

| **Molecule** | **Molecular Structure** | **IP (eV)** | **EA (eV)** | **$E_g$ (eV)** |
|---|---|---|---|---|
| NPB* (D) | 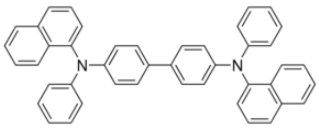 | 5.4 | 2.3 | 3.1 |
| m-TDATA[1] (D) | 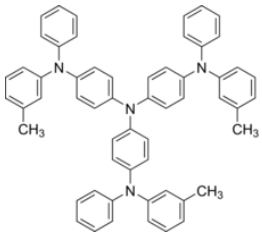 | 5.1 | 1.9 | 3.2 |
| TAPC[2] (D) | 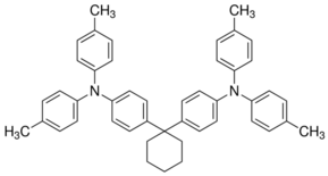 | 5.4 | 2.0 | 3.4 |
| TPD[3] (D) | 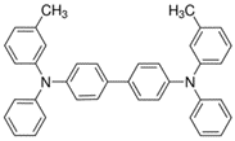 | 5.4 | 2.4 | 3.0 |
| PVK[4] (D) | 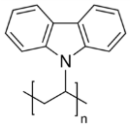 | 5.4 | 1.9 | 3.5 |
| HAT-CN* (A) | 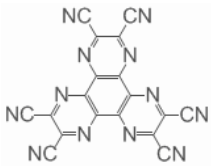 | 9.5 | 5.7 | 3.8 |
| NTCDA[5] (A) | 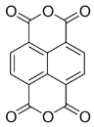 | 8.0 | 4.0 | 4.0 |

*From ultraviolet photoelectron spectroscopy and inverse photoemission spectroscopy measurements on thin films.

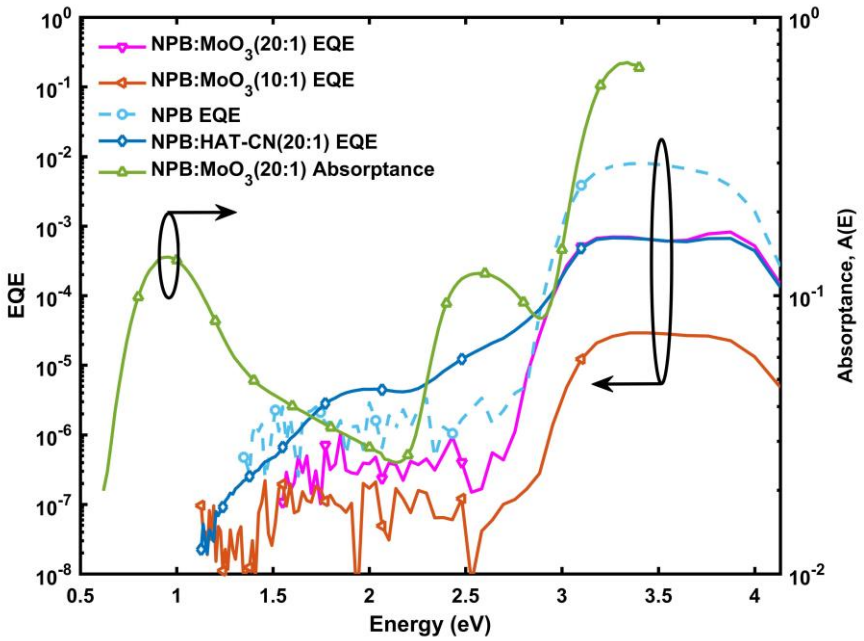


**Figure S1.** External quantum efficiency (EQE) spectra of devices comprising NPB doped with $MoO_3$ at two different concentrations. The EQE from a single layer of NPB is shown by the light blue dashed line. The EQE of NPB:$MoO_3$ (20:1) (magenta) and NPB:$MoO_3$ (10:1) (brown) devices both show only the photocurrent from NPB Frenkel excitons, with no contribution from the NPB cation absorption. The absorptance of NPB:$MoO_3$ (20:1) film (light green) and NPB:HAT-CN (20:1) device EQE (dark blue) is also shown for reference.

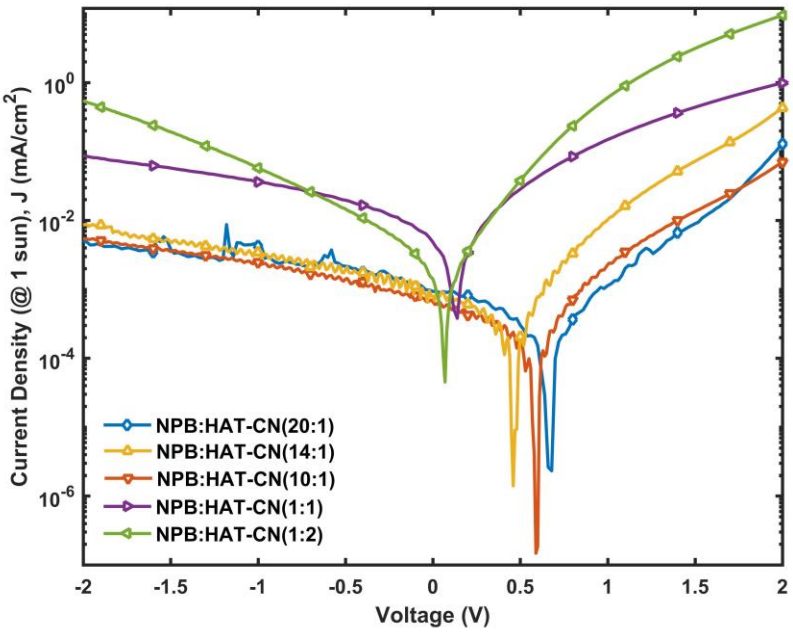


**Figure S2.** Current density-voltage characteristics of different blends of NPB:HAT-CN under AM1.5G (1 sun) illumination. The HAT-CN concentration was varied from 4.5 (dark blue, 20:1) to 67 vol% (light green, 1:2).

**Table S2.** Open-circuit voltage ($V_{OC}$) of different blends of NPB:HAT-CN under AM1.5G (1 sun) illumination. With HAT-CN concentration varying from 4.5 (20:1) to 67 vol% (1:2), $V_{OC}$ changes from 0.68 V to 0.07 V.

| **NPB:HAT-CN blend ratio (D:A) by volume** | $V_{OC}$ (V) |
|---|---|
| 20:1 | 0.68 |
| 14:1 | 0.46 |
| 10:1 | 0.59 |
| 1:1 | 0.14 |
| 1:2 | 0.07 |

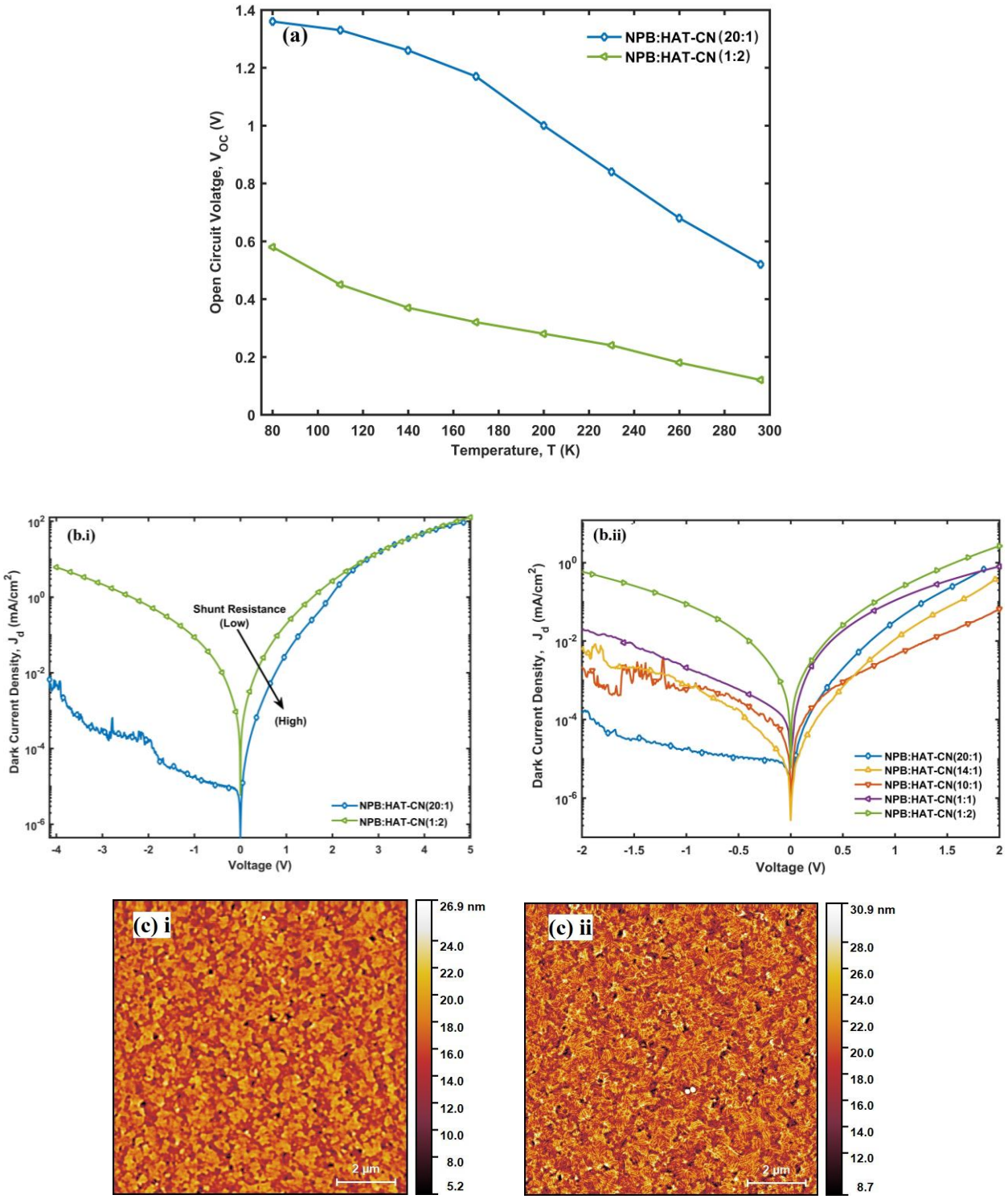


**Figure S3.** (a) Temperature dependent open-circuit voltage ($V_{OC}$) of 20:1 and 1:2 NPB:HAT-CN blend devices. The $V_{OC}$ of the 20:1 device (dark blue) increases linearly until reaching a saturation temperature at approximately 160 K, indicating a decrease of both charge carrier generation and competing recombination losses. The $V_{OC}$ of the 1:2 blend (light green) rises

continuously as temperature goes down. Note, the room temperature $V_{OC}$ is slightly different than the value shown in Table S2 due to device to device variation. (b) Room temperature dark current density-voltage characteristics of NPB:HAT-CN devices with different blend ratios, at (i) extended bias voltage from -4 V to 5 V and (ii) moderate bias voltage from -2 V to 2 V. Doping induced increased conductivity in devices with high HAT-CN concentration contributes to the large dark current at both forward and reverse bias, i.e. devices are shunted. (c) Atomic force microscope images of 100 nm thick films of NPB:HAT-CN (i) 20:1 and (ii) 1:2 blends, revealing r.m.s. surface roughness of 2.63 nm and 3.35 nm, respectively. Both follow the morphology of the ITO layer underneath.

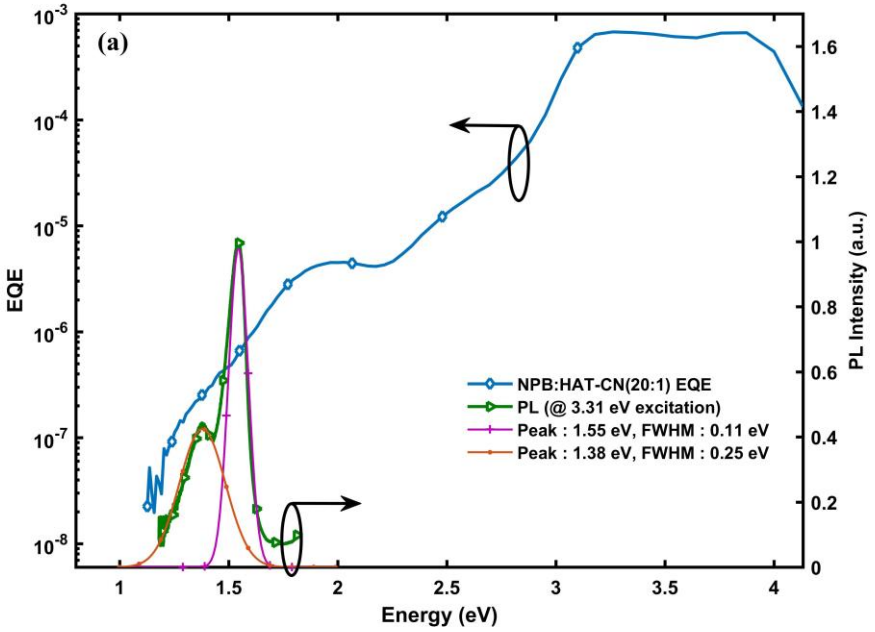
(a)
EQE
PL Intensity (a.u.)
Energy (eV)
NPB:HAT-CN(20:1) EQE
PL (@ 3.31 eV excitation)
Peak : 1.55 eV, FWHM : 0.11 eV
Peak : 1.38 eV, FWHM : 0.25 eV

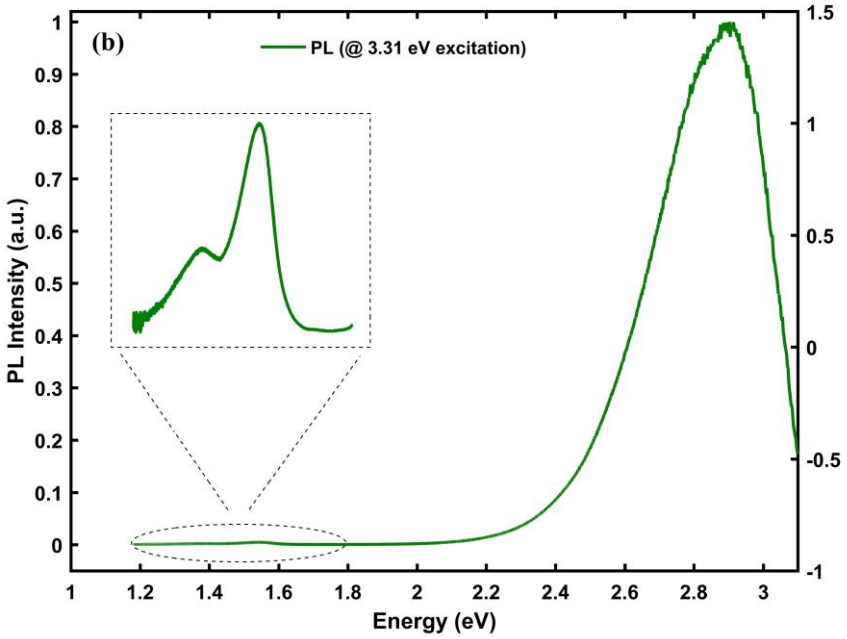
(b)
PL (@ 3.31 eV excitation)
PL Intensity (a.u.)
Energy (eV)

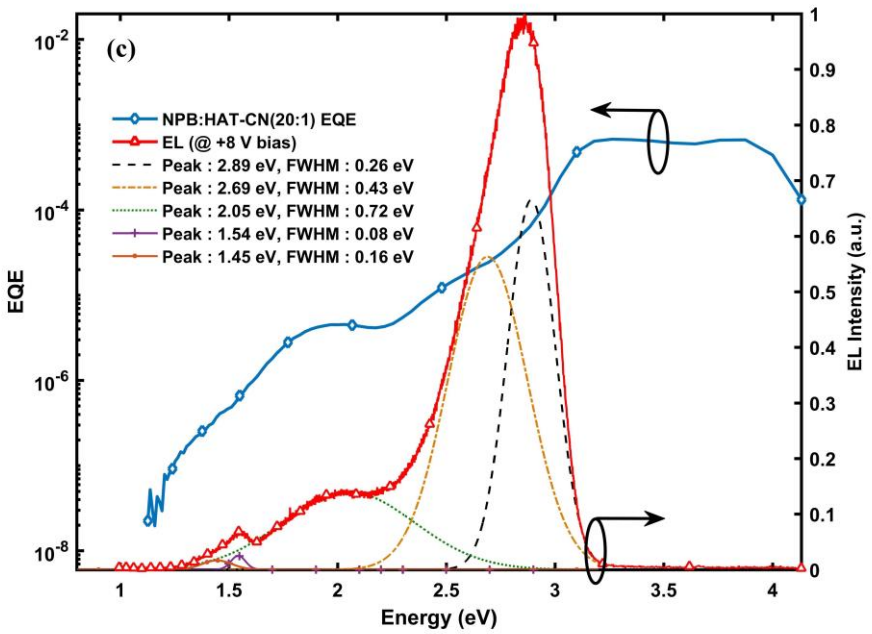


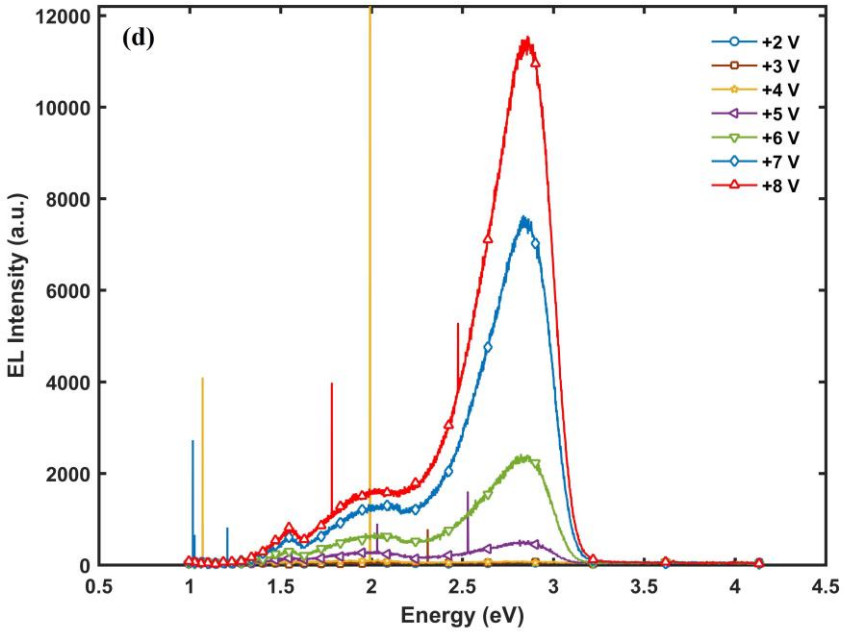


**Figure S4.** (a) Photoluminescence (PL) spectrum of NPB:HAT-CN(20:1) film for 3.31 eV (wavelength, λ = 375 nm) excitation (green solid line) and EQE of NPB:HAT-CN(20:1) device at short circuit condition (blue solid line). The PL spectrum can be fit with two Gaussian functions centering at 1.55 eV (purple solid line) and 1.38 eV (brown solid line), with full width at half maximum (FWHM) of 0.11 eV and 0.25 eV, respectively. (b) Complete PL spectrum of NPB:HAT-CN(20:1) film for 3.31 eV (wavelength, λ = 375 nm) excitation, showing NPB singlet

emission at around 2.9 eV and the low energy emission mentioned in (a) (exaggerated in the inset). InGaAs detector was also used to check PL emission down to 0.8 eV (not shown), but no emission was observed below the 1.38 eV and 1.55 eV peaks. (c) Electroluminescence (EL) spectra of NPB:HAT-CN(20:1) device at +8 V bias (red solid line) and EQE for the same device at short circuited condition (blue solid line). The EL spectrum can be fit with Gaussian functions centering at 2.89 eV (black dashed line), 2.69 eV (golden dashed line), 2.05 eV (green dashed line), 1.54 eV (purple solid line) and 1.45 eV (brown solid line), with FWHM of 0.26 eV, 0.43 eV, 0.72 eV, 0.08 eV and 0.16 eV, respectively. (d) Complete EL spectra of NPB:HAT-CN(20:1) device for +2 V to +8 V bias.

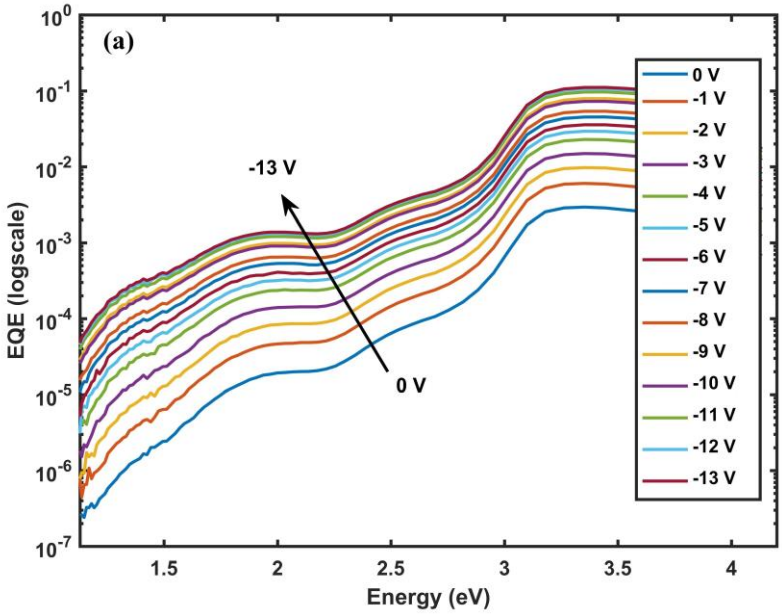
(a)
EQE (logscale)
Energy (eV)
-13 V
0 V
0 V
-1 V
-2 V
-3 V
-4 V
-5 V
-6 V
-7 V
-8 V
-9 V
-10 V
-11 V
-12 V
-13 V

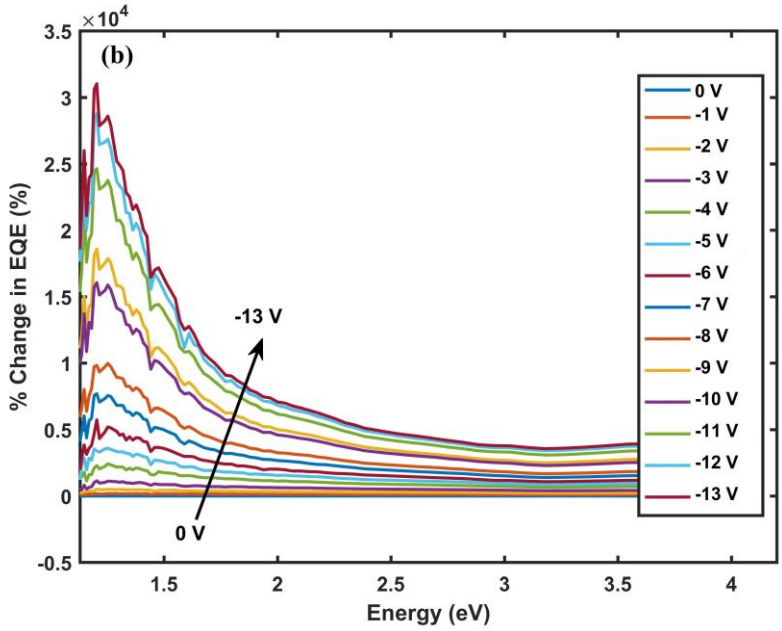
(b)
×10^4
% Change in EQE (%)
Energy (eV)
-13 V
0 V
0 V
-1 V
-2 V
-3 V
-4 V
-5 V
-6 V
-7 V
-8 V
-9 V
-10 V
-11 V
-12 V
-13 V

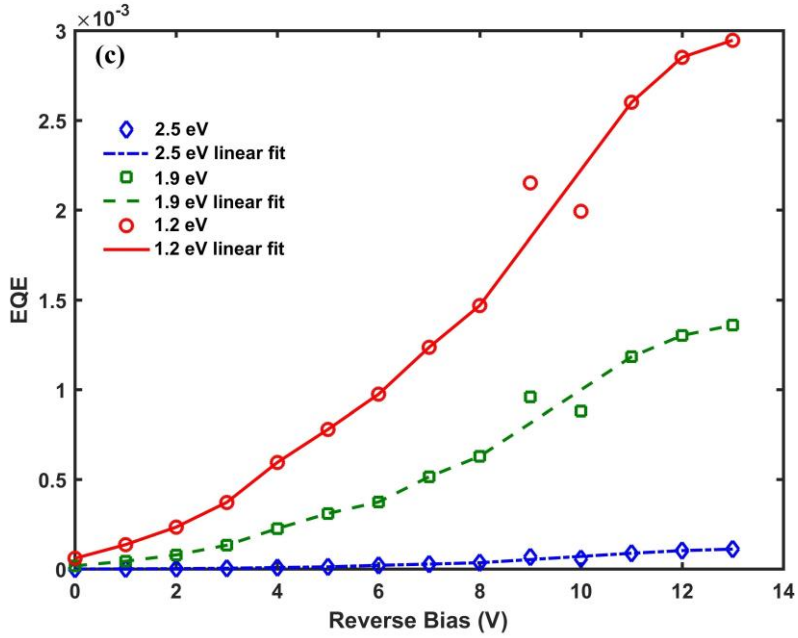


**Figure S5.** (a) External quantum efficiency (EQE) of NPB:HAT-CN(20:1) under pulsed square wave reverse bias from 0 V to 13 V (1 kHz, 50% duty cycle). With increasing reverse bias, the EQE continuously increases before starting to saturate above 10 V. (b) Percent change in EQE of the same device, showing lowest energy CT state is more strongly affected by the applied bias compared to higher energy CT states and Frenkel region. (c) EQE of the $CT_1$ (red), $CT_2$ (green) and $CT_3$ (blue) regions at different applied reverse bias. The saturation of the EQE above 10 V reverse bias indicates that almost all the absorbed photons are converted to charge and collected, meaning EQE become absorption limited.

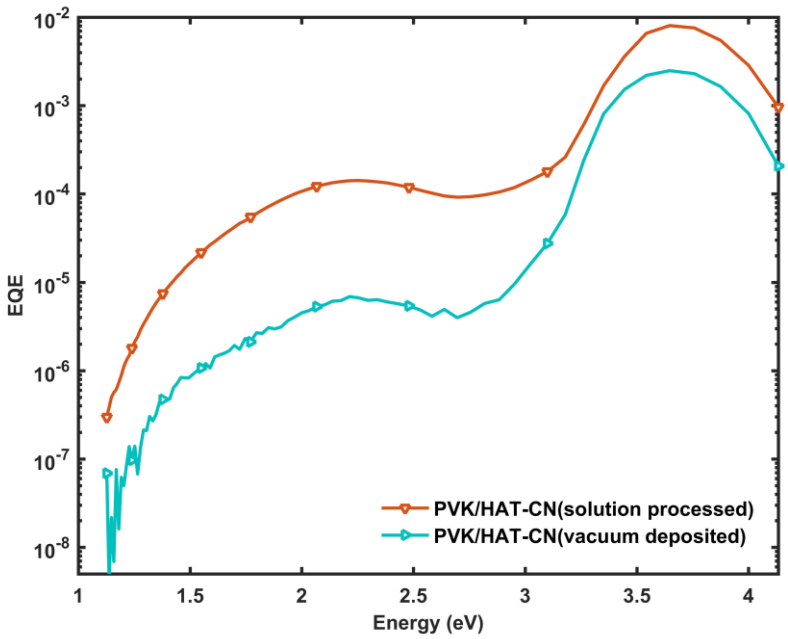


**Figure S6.** External quantum efficiency (EQE) spectra of PVK/HAT-CN planar heterojunction solar cells with solution processed PVK layers. Devices with solution processed (brown) and vacuum deposited (aqua) HAT-CN layer both display similar CT spectra.

## Electronic Structure Calculations

Gas-phase GW calculations were performed with the Fiesta code,[6,7] starting from ground-state DFT calculations, based on the PBE0 functional, obtained with the ORCA[8] package. A partial self-consistent scheme on the eigenvalues (evGW) was exploited, along with Gaussians basis set of the Dunning's correlation-consistent family[9] (cc-pVXZ, where X = 2, 3). Then, quasi-particle energy levels were extrapolated to the complete basis set (CBS) limit. The universal Weigend Coulomb[10] fitting set of functions was used as auxiliary basis in the resolution of identity (RI-V) approach.[11] The frontier orbitals of NPB and HAT-CN are reported in Table S3.

**Table S3.** Energy levels (in eV) of the NPB and HAT-CN isolated molecules obtained from ev*GW* calculations in the gas-phase. The molecular geometries were taken from the respective crystal structures.[12] Results for NPB were taken from Ref. 7. Note that IP = $-E_{HOMO}$, EA = $-E_{LUMO}$.

| NPB | | HAT-CN | |
|---|---|---|---|
| HOMO | -6.50 | LUMO | -3.59 |
| HOMO-1 | -7.32 | LUMO+1 | -3.42 |
| | | LUMO+2 | -3.47 |

MicroElectrostatic (ME) calculations were parametrized with ESP atomic charges[13] and polarizability tensor calculated with DFT at the ωB97X-D/6-311++G(d,p) level. ESP charges were computed for all neutral and charged molecules in the MD sample. The polarizability tensor was calculated for a neutral NPB and HAT-CN reference molecule and the polarizability of charged species was set equal to that of neutral ones. Polarization energies for holes ($\Delta^+$) and electron ($\Delta^-$) were calculated for spherical clusters and extrapolated to the bulk limit. The solid-state energy levels for holes on NPB and electrons on HAT-CN EA can be expressed as

$$E^s_{H-i} = E^g_{H-i} + \Delta^+ \ (i\text{=0,1}), \tag{S1}$$

$$\text{and } E^s_{L+j} = E^g_{L+j} + \Delta^- \ (j\text{=0,1,2}), \tag{S2}$$

respectively, where the subscript H/L are abbreviations for HOMO/LUMO and $E^g_k$ is the energy of the level $k$ in the gas phase (see Table S3.) Polarization energies are assumed to be level-independent. The distributions of solid-state energy levels obtained from the sampling of the MD morphologies are shown in Fig. S7. The statistics includes only molecules in the bulk region, i.e. it excludes the molecules within 4 nm from the substrate and vacuum interface.

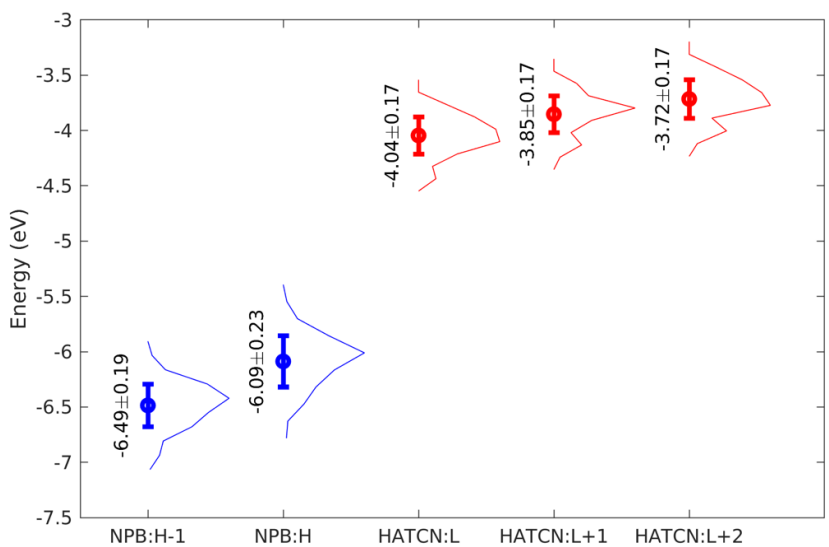


**Figure S7.** Distributions of the energy levels of the frontier orbitals of NPB (blue lines) and HAT-CN (red lines) in the blend calculated with our multiscale approach. Mean values and standard deviations are annotated and shown as error bars.

**Table S4.** Total orbital energy broadening (standard deviation $\sigma_{total}$, in eV) and its conformational ($\sigma_{conf}$) and electrostatic ($\sigma_{elec}$) contributions for NPB and HAT-CN.

| NPB | | | | HAT-CN | | | |
|---|---|---|---|---|---|---|---|
| | $\sigma_{conf}$ | $\sigma_{elec}$ | $\sigma_{total}$ | | $\sigma_{conf}$ | $\sigma_{elec}$ | $\sigma_{totoal}$ |
| HOMO | 0.18 | 0.17 | 0.23 | LUMO | 0.07 | 0.15 | 0.17 |
| HOMO-1 | 0.12 | 0.17 | 0.19 | LUMO+1 | 0.06 | 0.15 | 0.17 |
| | | | | LUMO+2 | 0.05 | 0.15 | 0.17 |

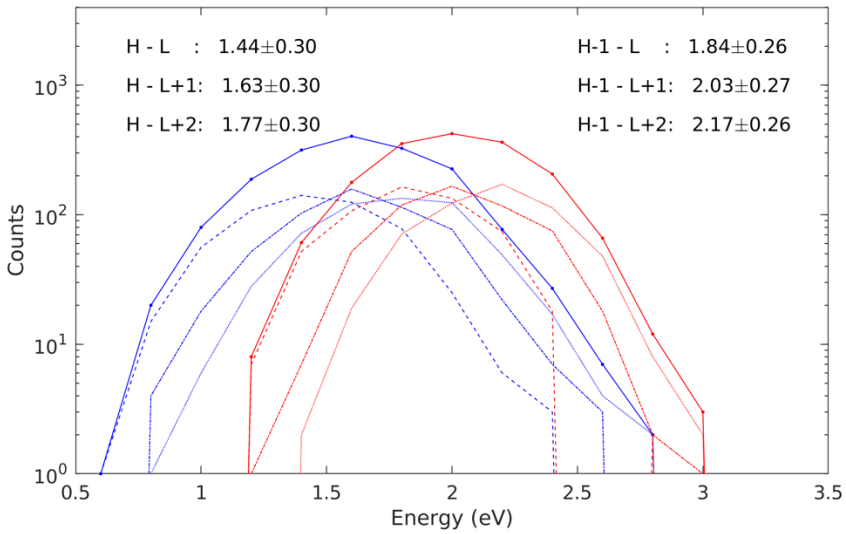


**Figure S8.** Distributions of CT energies (density of states, DOS) resolved into individual levels contributions. Red and blue solid lines correspond to CT transition from the NPB HOMO and HOMO-1 level, respectively. Dashed, dash-dotted and dotted lines correspond to transitions to the HAT-CN LUMO, LUMO+1, LUMO+2, respectively. Solid lines are obtained by summing up the counts to all the LUMOs (shown also in Fig. 3 main text). Mean values and standard deviations of each distribution are annotated.

Time-dependent DFT (CAM-B3LYP[14]/6-31G(d,p) level) calculations were performed for a few NPB-HAT-CN dimers extracted from the MD sample. The effect of the dielectric medium was accounted for within the polarizable continuum model (PCM)[15]. The absorption spectra of two dimers in Fig. S9 confirm the excitation pattern described in the main text, i.e. the presence of two series of three CT transitions from NPB-HOMO to HAT-CN LUMOs and a second analogous series arising from the NPD HOMO-1. The transition energies and oscillator strength are modulated by the changes in the molecular conformations.

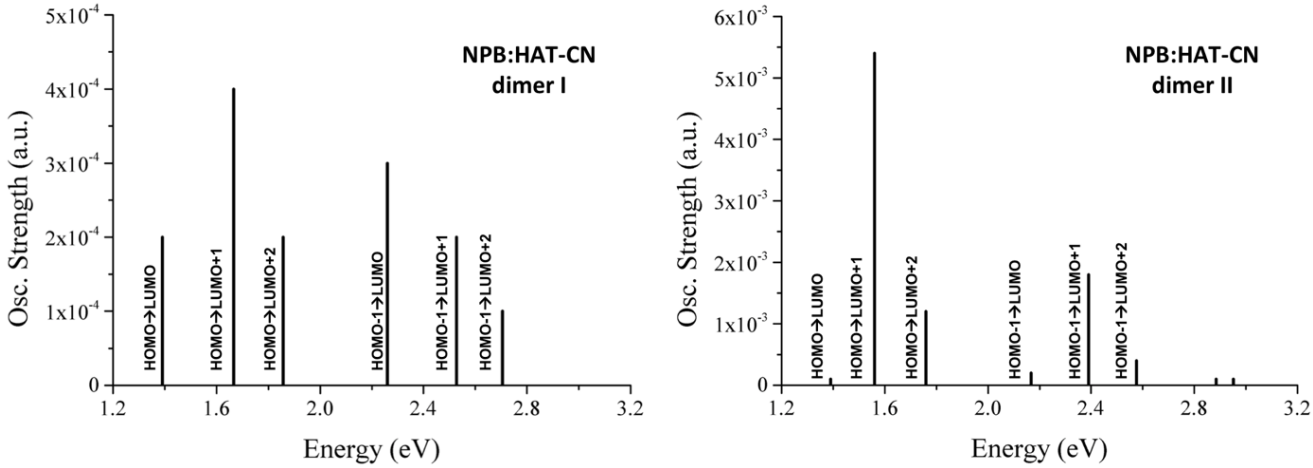


**Figure S9.** Absorption spectra of two NPB-HAT-CN dimers extracted from the MD samples (dimer I is the same for which results are shown in the main text) calculated at the TD-DFT level.

## References


(1) Wang, D.; Li, W.; Chu, B.; Su, Z.; Bi, D.; Zhang, D.; Zhu, J.; Yan, F.; Chen, Y.; Tsuboi, T. Highly Efficient Green Organic Light-Emitting Diodes from Single Exciplex Emission. *Appl. Phys. Lett.* **2008**, *92*, 053304.

(2) Wang, Y.; Liang, Q.; Huang, J.; Ma, D.; Jiao, Y. Investigation of the Hole Transport Characterization and Mechanisms in Co-Evaporated Organic Semiconductor Mixtures. *RSC Adv.* **2017**, *7*, 28494–28498.

(3) Lee, D.-H.; Liu, Y.-P.; Lee, K.-H.; Chae, H.; Cho, S. M. Effect of Hole Transporting Materials in Phosphorescent White Polymer Light-Emitting Diodes. *Org. Electron.* **2010**, *11*, 427–433.

(4) Gong, X.; Lim, S.-H.; Ostrowski, J. C.; Moses, D.; Bardeen, C. J.; Bazan, G. C. Phosphorescence from Iridium Complexes Doped into Polymer Blends. *J. Appl. Phys.* **2004**, *95*, 948–953.

(5) Falkenberg, C.; Uhrich, C.; Olthof, S.; Maennig, B.; Riede, M. K.; Leo, K. Efficient P-i-n Type Organic Solar Cells Incorporating 1,4,5,8-Naphthalenetetracarboxylic Dianhydride as Transparent Electron Transport Material. *J. Appl. Phys.* **2008**, *104*, 034506.

(6) Blase, X.; Attaccalite, C.; Olevano, V. First-Principles GW Calculations for Fullerenes, Porphyrins, Phtalocyanine, and Other Molecules of Interest for Organic Photovoltaic Applications. *Phys. Rev. B* **2011**, *83*, 115103.

(7) Li, J.; Duchemin, I.; Roscioni, O. M.; Friederich, P.; Anderson, M.; Da Como, E.; Kociok-Köhn, G.; Wenzel, W.; Zannoni, C.; Beljonne, D.; et al. Host Dependence of the Electron Affinity of Molecular Dopants. *Mater. Horizons* **2019**, *6*, 107–114.

(8) Neese, F. The ORCA Program System. *Wiley Interdiscip. Rev. Comput. Mol. Sci.* **2012**, *2*, 73–78.

(9) Dunning, T. H. Gaussian Basis Sets for Use in Correlated Molecular Calculations. I. The Atoms Boron through Neon and Hydrogen. *J. Chem. Phys.* **1989**, *90*, 1007–1023.

(10) Weigend, F. Accurate Coulomb-Fitting Basis Sets for H to Rn. *Phys. Chem. Chem. Phys.* **2006**, *8*, 1057-1065.

(11) Duchemin, I.; Li, J.; Blase, X. Hybrid and Constrained Resolution-of-Identity Techniques for Coulomb Integrals. *J. Chem. Theory Comput.* **2017**, *13*, 1199–1208.

(12) Szalay, P. S.; Galán-Mascarós, J. R.; Clérac, R.; Dunbar, K. R. HAT(CN)6: A New Building Block for Molecule-Based Magnetic Materials. *Synth. Met.* **2001**, *122*, 535–542.

(13) Besler, B. H.; Merz, K. M.; Kollman, P. A. Atomic Charges Derived from Semiempirical Methods. *J. Comput. Chem.* **1990**, *11*, 431–439.

(14) Yanai, T.; Tew, D. P.; Handy, N. C. A New Hybrid Exchange–Correlation Functional Using the Coulomb-Attenuating Method (CAM-B3LYP). *Chem. Phys. Lett.* **2004**, *393*, 51–57.

(15) Tomasi, J.; Mennucci, B.; Cammi, R. Quantum Mechanical Continuum Solvation Models. *Chem. Rev.* **2005**, *105*, 2999–3094.